CHEMISTRY OF MATERIALS

pubs.acs.org/cm

Article

Isotope Effect between H_2O and D_2O in Hydrothermal Synthesis

Xiuquan Zhou, Luning Wang, Xiulin Fan, Brandon Wilfong, Sz-Chian Liou, Yi Wang, Huafei Zheng, Zhange Feng, Chunsheng Wang, and Efrain E. Rodriguez*

Cite This: *Chem. Mater.* 2020, 32, 769–775

Read Online

ACCESS | Metrics & More | Article Recommendations | Supporting Information

ABSTRACT: Synthetic chemists can use different solvents (for example, polar vs nonpolar) to affect solute−solvent interactions and therefore favor a particular reaction product. Using a different isotope of the same solvent to select the product, however, is uncommon. We find that water and heavy water (D_2O) can select different products in the hydrothermal syntheses of iron-containing solids. Under hydrothermal and anaerobic conditions, water oxidizes iron to evolve hydrogen gas and a mixture of Fe^{2+}- and Fe^{3+}-containing solids. When we replace D_2O for H_2O under identical hydrothermal conditions, we can select thermodynamic products in our syntheses of iron-containing solids, whether it be oxides or chalcogenides. To explain this remarkable difference in product selectivity, we discover an unexpected difference in a fundamental property between H_2O and D_2O: their standard reduction potentials. Through electrochemical measurements and under strongly basic conditions (pH = 14), we find that the reduction potential of D_2O is 109 mV lower than that of H_2O. This difference in the reduction potential cannot be explained by the simple Nernst formulation. The unique product selectivity of D_2O over H_2O allows us to prepare iron chalcogenides with structures relevant to the iron-based superconductors.

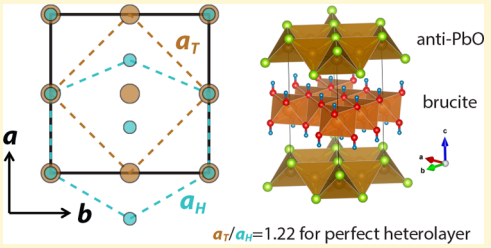

INTRODUCTION

Since Harold Urey isolated deuterium,[1] scientists have continuously discovered physical, chemical, and biological differences between normal water and heavy water, D_2O. Due to its heavier mass, D_2O displays the kinetic isotope effect,[2] which can even cause toxicity in organisms.[3] In studying chemical syntheses, chemists have elucidated reaction mechanisms by using the kinetic isotope effect.[4] However, up until now, no one has ever selected the thermodynamic product of a chemical reaction using D_2O instead of H_2O. If one could target products by choosing either H_2O or D_2O as the solvent, then a new avenue for synthesis becomes available for the materials chemist. This selectivity would be especially relevant for hydrothermal syntheses and many other reactions in the "universal solvent".

To our knowledge, no one has reported the differences between H_2O and D_2O under hydrothermal conditions to either prepare compounds or grow crystals. One can synthesize, dissolve, and crystallize a variety of inorganic solids through the hydrothermal technique, which heats water above 100 °C at pressures above 1 bar. This method gains its potency by changing several of water's properties such as its density and dielectric constant and therefore its solubility properties. Water's exceptionally large dielectric constant diminishes in size when heated beyond its boiling point and reaches that of a nonpolar solvent past its critical temperature. Given the difference in such physical properties (e.g., density) between D_2O and H_2O, pursuing hydrothermal synthesis with D_2O could reveal new inorganic solids previously inaccessible.

In earlier work[5] we had prepared an iron-based superconductor hydrothermally in both H_2O and D_2O for neutron measurement purposes. Specifically, we had prepared a deuterated version of the novel superconductor $(Li_{1-x}Fe_xOH)$-FeSe.[5] This heterolayered material separates $(FeSe)^{\delta-}$ layers by $(Li_{1-x}Fe_xOH)^{\delta+}$ layers, exhibits a critical temperature (T_c) of 43 K, and displays interesting physics due to the proximity of superconductivity with magnetism.[6−8] We used D_2O to form $(Li_{1-x}Fe_xOD)^{\delta+}$ layers in order to diminish incoherent scattering and absorption by hydrogen during the neutron scattering measurements. Unexpectedly, we found that the hydrothermal reactions with D_2O above 140 °C diminished the amount of Fe^{3+} oxide impurities, while using H_2O generated a significant amount of magnetic impurities such as Fe_3O_4.

We expand on our earlier hydrothermal work through systematic hydrothermal syntheses of iron-containing selenides in D_2O. The resulting products are also heterolayered materials that are obtained phase pure with D_2O but not H_2O. To understand the underlying cause for the differences seen in the products recovered from H_2O and D_2O, we have carried out a series of electrochemical studies on D_2O and H_2O. We obtain the reduction potential of both solvents at different pH levels. Since we carry out our hydrothermal syntheses under strongly

Received: October 8, 2019
Revised: January 3, 2020
Published: January 6, 2020

https://dx.doi.org/10.1021/acs.chemmater.9b04121
Chem. Mater. 2020, 32, 769–775

basic conditions, these pH studies are key to understanding the product selectivity afforded by D_2O over H_2O. We also briefly describe the unique crystal chemistry that arises from interleaving layered metal hydroxides with FeSe layers and report their magnetic properties.

EXPERIMENTAL SECTION

Hydrothermal Syntheses in H_2O and D_2O. For this work, we carried out hydrothermal syntheses of iron selenide layers intercalated by metal hydroxide sheets. We used KOH as the base and mineralizer, iron metal powder for the Fe^{2+} source, and selenourea as the SeH^- source for the formation of the FeSe layer; a variety of transition metals plus aluminum and zinc were used for the formation of the layered double hydroxides. We heated our hydrothermal autoclaves between 180 and 200 °C for 3−4 days using both H_2O and D_2O. For a typical synthesis of the target $[(M_{1-x}Al_x)(OH)_2]FeSe$ phases (where M include the metals Zn, Mg, Co, Ni, Fe, and Mn), approximately 10 mmol of Fe powder, 7−8 mmol of M powder, 4−5 mmol of granular Al, 15 mmol of selenourea, and 1.6−2 g of KOH were mixed with 25 mL of deionized (DI) water or D_2O (99%).

Both the H_2O and D_2O for the hydrothermal syntheses were degassed before use in order to remove any dissolved O_2 gas. The mixtures were transferred into a 45 mL Teflon-lined stainless steel autoclave under air-free conditions. Once sealed, the autoclave was heated to 180 °C for 4−5 days. Afterward, the content in the autoclave was washed and centrifuged several times under air-free conditions until the supernatant was clear. The remaining product was collected, vacuum-dried, and stored in an Ar-filled glovebox.

For the synthesis of pure KOD, potassium cubes (0.98 g, 25 mmol) were loaded in a Schlenk flask with a stirring bar in a glovebox. The flask was then transferred to a Schlenk line under Ar flow where it was loaded with about 20 mL of anhydrous tetrahydrofuran (THF). By use of a cold bath of a liquid nitrogen/ethanol mixture, the solution was cooled to −30 °C. Excess H_2O (about 4 g) was then added to the flask dropwise. After the K cubes were completely dissolved, the solution was allowed to warm up slowly to room temperature and stirred for 1 h. White powders were obtained upon the removal of THF and residue D_2O at room temperature by vacuum. The white powder was further degassed under vacuum at 180 °C for 5 h to remove any residual solvents.

Structural Studies. Powder X-ray diffraction (XRD) data were collected using a Bruker D8 X-ray diffractometer with Cu Kα radiation, λ = 1.5418 Å. Microscopic images were examined on a Hitachi SU-70 SEM field emission scanning electron microscope (SEM), and their elemental compositions were determined by energy dispersive X-ray spectroscopy (EDS) using a BRUKER EDS detector. Electron diffraction patterns were obtained using a JEM 2100 LaB_6 transmission electron microscope (TEM) at an acceleration voltage of 200 keV. Electron diffraction patterns were analyzed using the software ImageJ.

Reduction Potential Measurements. A Hg/HgO electrode in 20% KOH/H_2O (0.098 V) and a Hg/Hg_2Cl_2 electrode in saturated KCl solution (0.241 V) were used as reference electrodes (RF) for basic and acidic conditions, respectively. Solutions of 1 M KOH in H_2O and 1 M KOD in D_2O were prepared by dissolving stiochiometric amounts of anhydrous KOH or KOD using H_2O or D_2O, respectively, in volumetric flasks. The solutions of 1 M HCl and DCl were prepared by diluting 35% of concentrate HCl or 35% DCl in D_2O (Sigma-Aldrich) with H_2O or D_2O, respectively. All experiments were performed using a Pt foil as a working electrode and a Au foil as the counter electrode at a scanning rate of 5 mV/s.

Physical Properties Measurements of Layered Iron Selenides. To check for superconductivity and characterize any long-range magnetic ordering, magnetic susceptibility measurements of the iron selenides were performed using a quantum design magnetic properties measurement system (MPMS).

RESULTS AND DISCUSSION

Water as Oxidizing Agent under Anaerobic Hydrothermal Conditions. We first elucidate the special role water plays beyond that of a solvent in the reaction scheme of this study. Highly basic conditions established by saturating an aqueous solution with LiOH (or LiOD) can oxidize iron metal according to the Pourbaix diagram.[9] We draw a useful analogy to the formation of rust. In electrochemical corrosion, iron acts as the anode, air as the cathode, and the salt water as the electrolyte. In the present case, however, we rigorously exclude all oxygen from the hydrothermal apparatus. In place of oxygen, water itself must necessarily be the oxidizer. We therefore propose that the hydrothermal process is equivalent to electrochemical corrosion of iron. The anode here is the half-reaction $Fe|Fe(OH)_2$ and the cathode is $H_2O|H_2$. The high amount of LiOH (aq) acts as the mineralizer and electrolyte.

To help understand the redox chemistry under hydrothermal conditions, we expand the half-reactions $Fe|Fe(OH)_2$ and $H_2O|H_2$ fully in eqs 1 and 2. The overall cell reaction is then given by eq 3. The respective standard potentials[10] are included for all three reduction equations.

$$Fe(s) + 2OH^-(aq) \rightleftharpoons Fe(OH)_2(s) + 2e^- \quad E^\ominus = 0.89\ V \tag{1}$$

$$2H_2O(l) + 2e^- \rightleftharpoons H_2(g) + 2OH^-(aq) \quad E^\ominus = -0.828\ V \tag{2}$$

$$Fe(s) + 2H_2O(l) \rightleftharpoons Fe(OH)_2(s) + H_2(g) \quad E^\ominus = 0.062\ V \tag{3}$$

The overall cell reaction of eq 3 reveals a small yet positive value for the standard potential $E^\ominus$. Despite a small driving force, we can further push the equilibrium toward the products by increasing the temperature, which we do so under hydrothermal conditions where $T > 180°$. First, the Fe metal is gradually digested to Fe^{2+} (aq) in the form of $Fe(OH)_2$. Next, $Fe(OH)_2$ reacts with SeH^- (aq) produced by the decomposition of selenourea, to evolve FeSe layers. However, if the Fe metal is completely converted to $Fe(OH)_2$ (s), then we risk pushing the reaction toward the formation of Fe^{3+} oxides instead.

As shown in eq 4, $Fe(OH)_2$ can also readily reduce water, and the standard potential $E^\ominus$ of this reaction is even smaller than that of eq 3. Therefore, if Fe^{2+} (aq) species react with SeH^- (aq) before any $Fe(OH)_2$ (s) can convert into Fe^{3+}-containing oxides, then we have a higher probability of forming phase pure FeSe (s). Indeed, in our earlier work we found that by simply omitting the source of SeH^- (selenourea), we could form pure Fe_3O_4 under hydrothermal conditions.[5] Similar experiments over the course of 1 and 2 days were also carried out in this study to understand what happens to Fe metal without any complexing anions such as SeH^- or SH^- in solution. We find that the D_2O hydrothermal reactions afford less amounts of Fe^{3+}-containing oxides after 1 d (Figure S1a). More interestingly, an apparent layered phase arises after 2 d reaction in D_2O while absent from the same reaction in H_2O (Figure S1b). This layer phase is likely a type of layered double hydroxide of $Fe(OH)_2$ consisting of predominately Fe^{2+}. These results clearly demonstrate that the differences between hydrothermal synthesis in H_2O and D_2O are beyond simple kinetic effects but thermodynamic ones as well.

https://dx.doi.org/10.1021/acs.chemmater.9b04121
Chem. Mater. 2020, 32, 769−775

$$2Fe(OH)2(s) \rightleftharpoons Fe_2O_3(s) + H_2O(l) + H_2(g) \quad E^{\ominus} = 0.032\ V \tag{4}$$

The Standard Reduction Potential of D_2O Is Lower than H_2O at pH = 14. Once water's role as both solvent and reactant is understood, one can formulate a testable hypothesis on why heavy water should yield a different product during hydrothermal synthesis. We hypothesize that D_2O has a lower reduction potential than H_2O in strong base. In other words, the standard potential of eq 2 must be significantly lower for D_2O than H_2O in order to effect the $E^{\ominus}$ of both eq 3 and eq 4. While electrolysis of D_2O has long been known,[1] only the standard potential of D^+ (aq) has been reported. Compared to the $2H^+|H_2$ half-reaction, the $2D^+|D_2$ half-reaction is 13 mV lower.[10]

We report here for the first time the $D_2O|D_2$ half reaction in base. We carried out this electrochemical measurement with 1 M KOD in D_2O and 1 M KOH in H_2O. Since the reduction potential is pH-dependent, we also performed the measurement for 1 M HCl and 1 M DCl as a control. Remarkably, we found the reduction potential of D_2O to be 109 mV lower than that of H_2O in alkaline media. Such a large difference is unexpected since the predicted difference using the Nernst equation is merely 65 mV (detailed calculation in Supporting Information). Our result indicates a different and more complex mechanism for the electrochemical reduction of D_2O.

Figure 1a shows the clear difference between the reduction potentials of D_2O and H_2O for high pH, whereas the small difference found at low pH is consistent with previous reports. Figure 1b gives the comparison between different iron species in base with regard to both H_2O and D_2O. We provide the standard reduction potential for D_2O in basic conditions below.

$$2D_2O(l) + 2e^- \rightleftharpoons D_2(g) + 2OD^-(aq) \quad E^{\ominus} = -0.935\ V \tag{5}$$

Product Selectivity of D_2O over H_2O. Now that we have established that D_2O is more difficult to reduce than H_2O, we set out to design a series of hydrothermal syntheses under basic conditions. We continue our preparation of FeSe layers but now introduce a different metal hydroxide layer to intercalate them. Our motivation was twofold: (1) single layer FeSe deposited on a $SrTiO_3$ substrate exhibits a high T_c ranging from 65 to 100 K;[11,12] (2) layered double hydroxides with the brucite-type structure readily intercalate a wide variety of anionic species from polymers to biomolecules to organometallic complexes.[13] Typically, such layered hydroxides are formulated $(M_{1-x}M'_x(OH)_2)^{\delta+}$ where M is a divalent metal and M′ a trivalent metal so that the overall layer is cationic. We present results for hydrothermal reactions incorporating Mg^{2+}, Fe^{2+}, Co^{2+}, Ni^{2+}, and Zn^{2+}.

First, we discuss our results for hydrothermal synthesis with H_2O. We find that attempts with Co and Ni metal do not yield any new compounds but instead unreacted metal and reagents. This result makes sense since the standard reduction potentials for $Co(OH)_2|Co$ (−0.746 V) and $Ni(OH)_2|Ni$ (−0.716 V) are too high to be surmounted by water's reduction potential (Figure 1b).[10] In the case of M = Zn, we find that zinc is readily digested by water. However, Zn^{2+} is a softer Lewis acid than Fe^{2+}, and it therefore competes for SeH^- groups. Subsequently, we only formed ZnSe and no iron selenides of any kind. For the other metals, we recovered samples with a large amount of magnetic oxide impurities. After removal of these impurities with a bar magnet, the yield fell by more than 50%. By powder X-ray diffraction (XRD), we found the remaining product to consist mostly of $M(OH)_2$, $K_xFe_{2-y}Se_2$, and a minor unidentified phase (Figure 2a). We conclude that reactions in H_2O yielded products with a mixture of Fe^{2+}/Fe^{3+}.

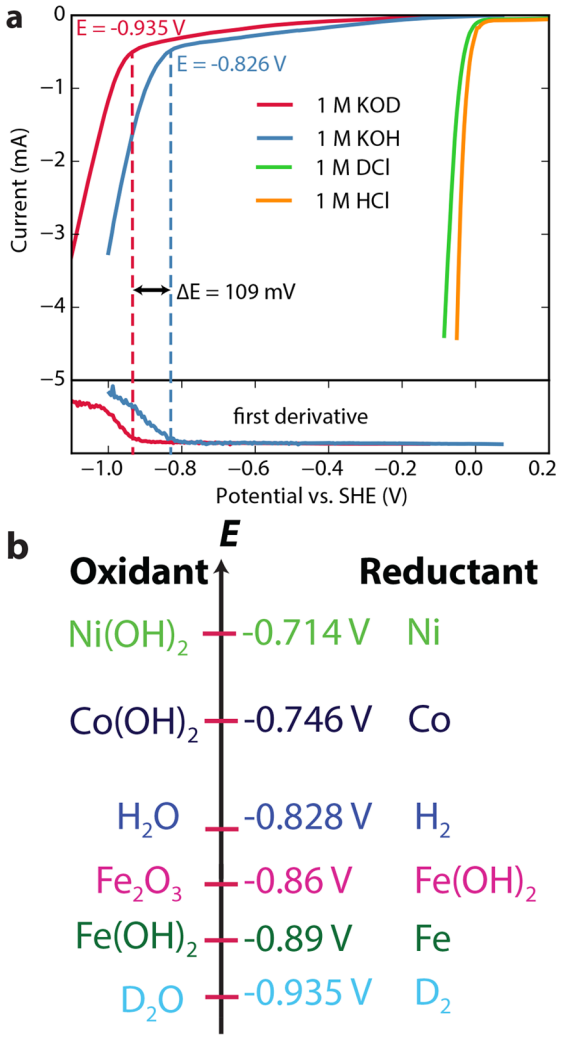

Figure 1. Electrochemical potentials in base. (a) Hydrogen evolution potential of H_2O and D_2O against standard hydrogen electrode (SHE). The potentials in 1 M base and 1 M acid were measured using a Hg/HgO and Hg/Hg_2Cl_2 reference electrodes, respectively. The onsite potentials for H_2O and D_2O in base were obtained at the point when their respective first derivate changed. (b) Standard reduction potentials of metal hydroxide in comparison to H_2O and D_2O.

For the same conditions described above when we used D_2O in place of H_2O, we found some similarities yet striking differences in the reaction products. First, the similarities: When using M = Co, Ni, and Zn metals in D_2O, we were also left with either unreacted metal or the formation of ZnSe. The major difference came when we incorporated Mg into the hydrothermal reaction. We recovered samples that consisted of a new phase by powder XRD (Figure 2a).

From electron microscopy images, this new phase is highly micaceous and its morphology is that of flat sheets or scroll-like tubes (Figure 2b,c). We observe lattice fringes of approximately 5.5 Å (Figure 2d), which would correspond to approximately twice the Fe−Fe distance in pristine FeSe, indicating a superstructure with respect to its tetragonal cell.

https://dx.doi.org/10.1021/acs.chemmater.9b04121
Chem. Mater. 2020, 32, 769−775

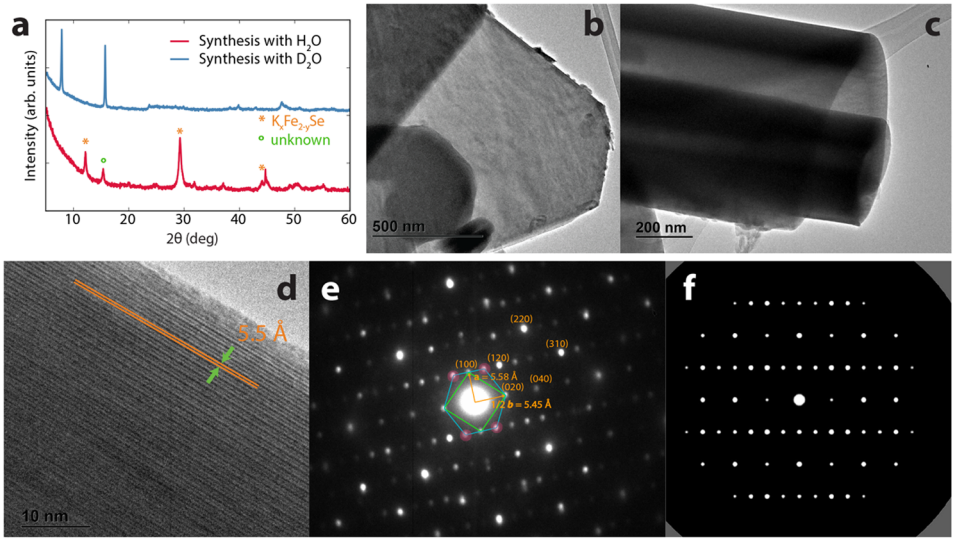

Figure 2. Structural characterization of $[(Mg_{1-x}Al_x)(OH)_2]FeSe$. (a) XRD for identical samples synthesized using H_2O and D_2O, respectively. The sample prepared using H_2O contained mainly $K_{2x}Fe_{2-x}Se_2$ and an unknown phase. (b, c) Different morphologies for $[(Mg_{1-x}Al_x)(OD)_2]FeSe$ showing sheets and scrolls, respectively. (d) TEM image for $[(Mg_{1-x}Al_x)(OD)_2]FeSe$ showing a lattice fringe of about 5.5 Å, corresponding to the [100]-direction. (e) Projection of lattice points from a commensurate heterolayered structure exhibiting both 4-fold and 6-fold symmetries. The calculated lattice constants are a = 5.58 Å, $\frac{1}{2}b$ = 5.45 Å. There is a ×2 superstructure along b, and the superlattice reflections are highlighted in red circles. (f) Simulated electron diffraction pattern for the structure shown in part b, showing a nearly identical pattern to part e.

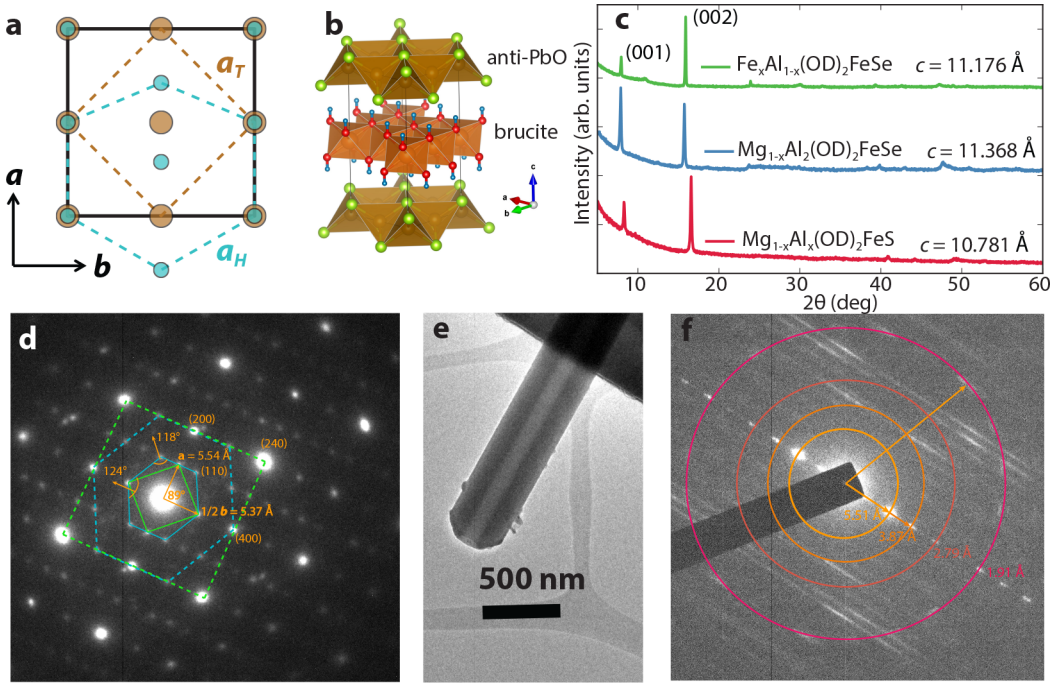

Figure 3. Structural characterization of $[(M_{1-x}Al_x)(OD)_2]FeSe$. (a) Projection of lattice points from a commensurate heterolayered structure exhibiting both 4-fold and 6-fold symmetries. (b) Structure model for $[(M_{1-x}Al_x)(OD)_2]FeSe$. (c) Powder X-ray diffraction for $[(M_{1-x}Al_x)(OD)_2]FeCh$. (d, e) Electron diffraction pattern and microscopy image showing a hollow nanotube for $[(Fe_{1-x}Al_x)(OD)_2]FeSe$. (f) Electron diffraction pattern of part e.

Both XRD and electron diffraction patterns (Figure 2e) clearly indicate that this phase is FeSe intercalated by another layer and more specifically one with pseudo-6-fold symmetry. The only suitable model to simulate the ED pattern (Figure 2f) was that of a mineral known as tochilinite, which incorporates FeS layers isostructural to FeSe with layered double hydroxides. We term this new phase seleno-tochilinite after the mineral, formulate its stoichiometry as $[Mg_{1-x}Al_x(OD)_2]FeSe$, and describe its crystal chemistry in the next section.

D_2O-Hydrothermal Stabilization of Seleno-tochilinite. Structurally, seleno-tochilinite consists of the layered double hydroxide $[Mg_{1-x}Al_x(OD)_2]^{\delta+}$ interleaved between $(FeSe)^{\delta-}$ layers (Figure 3a,b). In our previous work with iron sulfides,[14] we had isolated a similar phase, $[Na_{1-x}Fe_x(OH)_2]FeS$. The XRD patterns only show the

https://dx.doi.org/10.1021/acs.chemmater.9b04121
Chem. Mater. 2020, 32, 769−775

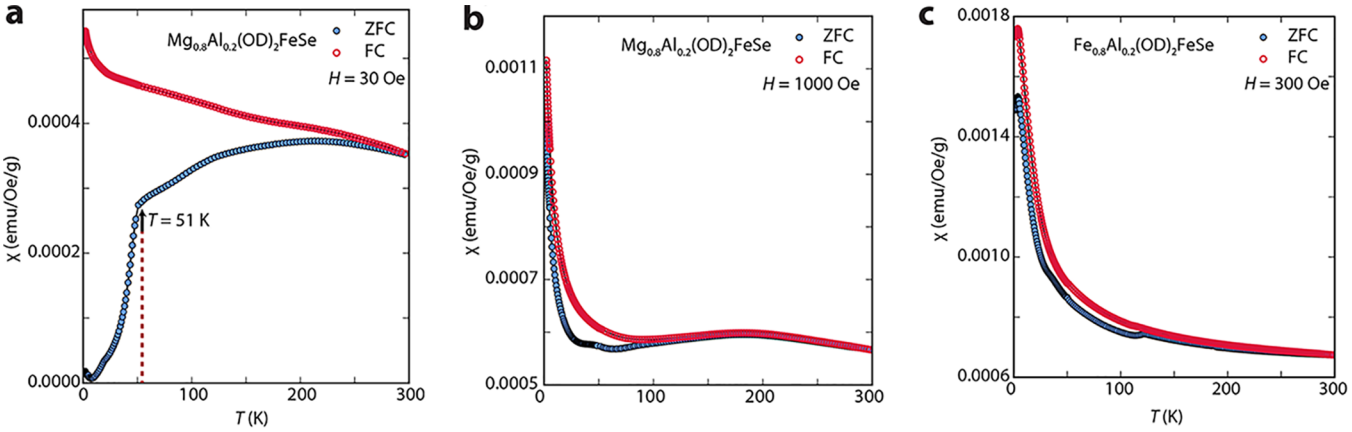

Figure 4. Magnetic susceptibility of $[(M_{1-x}Al_x)(OH)_2]FeSe$. (a, b) Mg at 30 and 1000 Oe, respectively. The transition at 51 K shown in part a is completely suppressed, suggesting possible filamentry superconductivity in the FeSe layers. (b) With higher applied fields, only paramagnetism is observed. (c) Likewise for M = Fe, the compound diplays only paramagnetism.

sharp (00*l*) reflections of seleno-tochilinite for M = Fe^{2+}, Mg^{2+} and M′ = Al^{3+} since the compound is disordered in the *ab*-plane but coherently stacked along the *c*-axis (Figure 3c). We also prepared the sulfide-based tochilinite as a reference to the new compounds. We only extract the lattice constant *c* from powder XRD patterns as presented in Figure 3c. The $Fe(OD)_2$-intercalated FeSe exhibits a smaller *c*-parameter than the $Mg(OD)_2$-intercalated one because the interlayer spacing in $Fe(OH)_2$ (4.605 Å [15]) is smaller than in $Mg(OH)_2$ (4.779 Å [16]).

The seleno-tochilinite, synthesized for the first time by using D_2O, expresses rare structural chemistry. The double hydroxide layer adopts the brucite structure and therefore contains a 6-fold rotational axis. The interleaved FeSe layer, however, is based on a different structure type with a 4-fold rotational axis. Nevertheless, we can stack these two disparate layers in a commensurate manner to form a true bulk heterostructure as evidenced by transmission electron diffraction (TED). We examine their (*hk*0) reflections along the [001]-axis in TED and clearly see diffraction patterns consisting of both square and hexagonal arrays (Figure 3d).

We formulate a simple geometrical argument as to why seleno-tochilinite can form these bulk heterostructures. To construct the smallest regular unit cell, we inscribe a tetragonal one and hexagonal one within a larger square cell (Figure 3a). The larger cell is a $\sqrt{2} \times \sqrt{2}$ superstructure of the tetragonal one with lattice constant a_T. If the hexagonal cell's lattice parameter is a_H, then we can define a tolerance factor τ as being the simple ratio a_T/a_H. To form an undistorted heterostructure, τ should be $\sqrt{3}/\sqrt{2} \simeq 1.22$. Therefore, the closer τ is to 1.22, the more compatible are the hexagonal and tetragonal the lattices.

With the tolerance factor τ defined for heterostructures of square and hexagonal layers, we can now understand how seleno-tochilinite crystallizes. For the hexagonal parameters a_H of $Mg(OH)_2$ and $Fe(OH)_2$, we calculate τ to be 1.199 and 1.159, respectively.[15,16] They are slightly below the ideal 1.22, but we remedy this by alloying the M-site with some Al^{3+} to increase τ. Without the inclusion of Al, we cannot stabilize seleno-tochilinite as the major product. Nevertheless, we do not form ideal heterostructures since the FeSe's square lattice becomes slightly distorted. The symmetry is lowered from 4-fold to 2-fold, and we now index the TED reflections with a $\sqrt{2} \times 2\sqrt{2}$ cell. We find the lattice parameters of this cell to correspond to a = 5.58 Å, $\frac{1}{2}b$ = 5.45 Å for Mg-intercalated seleno-tochilinite and a = 5.54 Å, $\frac{1}{2}b$ = 5.37 Å for the Fe-intercalated phase. We simulated the TED pattern of our heterostructured model and found it to match well the experimental pattern (Figure 2f).

Layered materials such as graphene[17] and phyllosilicates[18] can form a diverse array of microstructures. For example, the phyllosilicate known as chrysotile (i.e., asbestos) rolls up into fibers instead of stacking into sheets due to lattice mismatch and resulting strain.[19] Seleno-tochilinite also expresses such microstructural diversity. As seen from TEM images, seleno-tochilinite can roll into either hollow nanotubes (Figure 3e) or scroll-like tubes (Figure 2c). Energy dispersive X-ray spectroscopy (EDS) analysis suggests that particles of both morphologies, sheets and tubes, exhibit the same chemical composition (Figure S2). The TED pattern of this nanotube reveals strong Bragg reflections located at 5.51, 3.87, 2.79, and 1.91 Å; we index these spots as the (*hkl*) reflections of (100), (120), (200), and (240), respectively. The TED pattern, however, lacks any well-defined (0*k*0) reflections and displays streaking of the reflections along the [*h*00]-direction. Therefore, the seleno-tochilinite sheets curve along the *b*-direction, and the *a*-direction marks the nanotube axis. Likely, the distortion of the square lattice discussed earlier, whereby $\frac{1}{2}b < a$, strains the heterolayers and the curvature relieves it, much as in chrysotile and related phyllosilicates.

Magnetic Susceptibility of Intercalated Phases. None of the new intercalated phases where found to be superconducting. Instead, we found both $[(Mg_{1-x}Al_x)(OD)_2]FeSe$ and $[(Fe_{1-x}Al_x)(OD)_2]FeSe$ to exhibit paramagnetism at higher applied magnetic fields (*H*) (Figure 4). For *H* = 30 Oe, $[(Mg_{1-x}Al_x)(OD)_2]FeSe$ shows a transition at about 55 K in the zero field cooled (ZFC) curve, which is completely suppressed by increasing *H* to 1000 Oe. It is possible that this transition is indicative of filamentry superconductivity, or it could simply be due to uncompensated moments the ZFC curve due to a small applied field of 30 Oe. The absence of robust superconductivity could be a result of distortion of the square lattice or from overdoping of electrons from the cationic $[(Mg_{1-x}Al_x)(OD)_2]^{\delta+}$ layer. However, tuning the M/M′ ratio in these syntheses could lead to the optimal electron

https://dx.doi.org/10.1021/acs.chemmater.9b04121
Chem. Mater. 2020, 32, 769−775

doping into the FeSe layer while approaching the ideal tolerance factor τ. Such a compound could lead to the discovery of a new Fe-based superconductor.

CONCLUSIONS

Originally developed by geologists to digest and recrystallize minerals,[20] the hydrothermal method has matured over the past 150 years to include the synthesis of a diverse array of inorganic materials. The hydrothermal and the related solvothermal techniques[21,22] have been extensively used for the preparation of zeolites,[23] metal−organic frameworks,[24] oxides,[25] nanomaterials,[26] other inorganic solids. We show here that this technique still has the ability to surprise us, and the unexpected difference between H_2O-hydrothermal with D_2O-hydrothermal product selectivity demonstrates that there is new phase space to explore for materials synthesis. Not only are pH, temperature, volume, solute concentration, and pressure knobs to tune for targeting inorganic products but now also the ratio H_2O/D_2O in the solvent.

We have demonstrated with empirical evidence that the reduction potential difference between D_2O and H_2O is significant enough to utilize in chemical syntheses. The measured reduction potential of D_2O was obtained for the first time under highly basic conditions. For pH = 14, the reduction potential of D_2O is a remarkable 109 mV lower than that of H_2O. We exploited this significant difference for the hydrothermal synthesis of iron-containing solids with intriguing heterolayered structures.

While we have synthesized a particular set of compounds with D_2O that were difficult to isolate with H_2O, the methodology we employ could be used more generally in hydrothermal synthesis. For example, the unique reduction potentials of Fe^{2+} and Fe^{3+} could be exploited to carry out hydrothermal reactions of Fe metal in the presence of anions such as halides, pnictides, carbonates, carboxylates, and other ligands at high pH. In the present study we carried out these reactions in the presence of the anions SH^- and SeH^- to evolve bulk heterolayered materials that vertically stack materials with both 4-fold (in FeSe) and 6-fold (layered double hydroxide) symmetries. We found the cyrstal chemistry factors (e.g., the tolerance factor $\tau \simeq 1.22$) that allow for such symmetries to stack and can now design future tochilinite-type phases. Pure forms of these bulk heterostructures were made possible using D_2O over H_2O.

Finally, our findings cannot currently be explained by the kinetic isotope effect and should therefore spark mechanistic studies on why D_2O is so different from H_2O under alkaline conditions. The universal solvent still has new tricks to teach us as materials chemists for the preparation of functional materials, and fundamental studies on the solubility of inorganic species in D_2O and H_2O may lead to novel approaches for the precipitation and crystal growth of new phases.

ASSOCIATED CONTENT

Supporting Information

The Supporting Information is available free of charge at https://pubs.acs.org/doi/10.1021/acs.chemmater.9b04121.

Predicted potential, intercalation potentials, and elemental analysis (PDF)

AUTHOR INFORMATION

Corresponding Author

Efrain E. Rodriguez − *University of Maryland, College Park, Maryland;* orcid.org/0000-0001-6044-1543; Phone: (301) 405-1541; Email: efrain@umd.edu

Other Authors

Xiuquan Zhou − *University of Maryland, College Park, Maryland;* orcid.org/0000-0002-1361-3880

Luning Wang − *University of Maryland, College Park, Maryland*

Xiulin Fan − *University of Maryland, College Park, Maryland;* orcid.org/0000-0001-7294-480X

Brandon Wilfong − *University of Maryland, College Park, Maryland*

Sz-Chian Liou − *University of Maryland, College Park, Maryland*

Yi Wang − *University of Maryland, College Park, Maryland;* orcid.org/0000-0003-2309-3759

Huafei Zheng − *University of Maryland, College Park, Maryland*

Zhange Feng − *Argonne National Laboratory, Lemont, Illinois;* orcid.org/0000-0001-5793-0477

Chunsheng Wang − *University of Maryland, College Park, Maryland;* orcid.org/0000-0002-8626-6381

Complete contact information is available at: https://pubs.acs.org/10.1021/acs.chemmater.9b04121

Notes

The authors declare no competing financial interest.

ACKNOWLEDGMENTS

We thank Dr. Peter Zavalij at the University of Maryland for discussions on crystal structures. Research at the University of Maryland was supported by the NSF Career DMR-1455118 and the AFOSR Grant FA9550-14-1-0332. We also acknowledge support from the Maryland Nanocenter and Center for Nanophysics and Advanced Materials.

REFERENCES

(1) Urey, H. C.; Brickwedde, F. G.; Murphy, G. M. A Hydrogen Isotope of Mass 2. *Phys. Rev.* **1932**, *39*, 164−165.

(2) Bigeleisen, J.; Mayer, M. G. Calculation of Equilibrium Constants for Isotopic Exchange Reactions. *J. Chem. Phys.* **1947**, *15*, 261−267.

(3) Kushner, D. J.; Baker, A.; Dunstall, T. G. Pharmacological uses and perspectives of heavy water and deuterated compounds. *Can. J. Physiol. Pharmacol.* **1999**, *77*, 79−88.

(4) Baldwin, J. E.; Gallagher, S. S.; Leber, P. A.; Raghavan, A. S.; Shukla, R. Deuterium Kinetic Isotope Effects and Mechanism of the Thermal Isomerization of Bicyclo[4.2.0]oct-7-ene to 1,3-Cyclooctadiene. *J. Org. Chem.* **2004**, *69*, 7212−7219.

(5) Zhou, X.; Borg, C. K. H.; Lynn, J. W.; Saha, S. R.; Paglione, J.; Rodriguez, E. E. The preparation and phase diagrams of $(^7Li_{1-x}Fe_xOD)FeSe$ and $(Li_{1-x}Fe_xOH)FeSe$ superconductors. *J. Mater. Chem. C* **2016**, *4*, 3934−3941.

(6) Pachmayr, U.; Nitsche, F.; Luetkens, H.; Kamusella, S.; Brückner, F.; Sarkar, R.; Klauss, H.-H.; Johrendt, D. Coexistence of 3*d*-Ferromagnetism and Superconductivity in $[(Li_{1-x}Fe_x)OH]$-$(Fe_{1-y}Li_y)Se$. *Angew. Chem., Int. Ed.* **2015**, *54*, 293−297.

(7) Lu, X. F.; Wang, N. Z.; Wu, H.; Wu, Y. P.; Zhao, D.; Zeng, X. Z.; Luo, X. G.; Wu, T.; Bao, W.; Zhang, G. H.; Huang, F. Q.; Huang, Q.

Z.; Chen, X. H. Coexistence of superconductivity and antiferromagnetism in $(Li_{0.8}Fe_{0.2})$OHFeSe. *Nat. Mater.* **2015**, *14*, 325−329.
(8) Lynn, J. W.; Zhou, X.; Borg, C. K. H.; Saha, S. R.; Paglione, J.; Rodriguez, E. E. Neutron investigation of the magnetic scattering in an iron-based ferromagnetic superconductor. *Phys. Rev. B: Condens. Matter Mater. Phys.* **2015**, *92*, No. 060510.
(9) Beverskog, B.; Puigdomenech, I. Revised Pourbaix diagrams for iron at 25−300 °C. *Corros. Sci.* **1996**, *38*, 2121−2135.
(10) Vanysek, P. Electrochemical series. *CRC Handbook of Chemistry and Physics*; CRC, 1998; Vol. *87*.
(11) Liu, D.; Zhang, W.; Mou, D.; He, J.; Ou, Y.-B.; Wang, Q.-Y.; Li, Z.; Wang, L.; Zhao, L.; He, S.; et al. Electronic origin of high-temperature superconductivity in single-layer FeSe superconductor. *Nat. Commun.* **2012**, *3*, 931.
(12) Ge, J.-F.; Liu, Z.-L.; Liu, C.; Gao, C.-L.; Qian, D.; Xue, Q.-K.; Liu, Y.; Jia, J.-F. Superconductivity above 100 K in single-layer FeSe films on doped $SrTiO_3$. *Nat. Mater.* **2015**, *14*, 285−289.
(13) Khan, A. I.; O'Hare, D. Intercalation chemistry of layered double hydroxides: recent developments and applications. *J. Mater. Chem.* **2002**, *12*, 3191−3198.
(14) Zhou, X.; Eckberg, C.; Wilfong, B.; Liou, S.-C.; Vivanco, H. K.; Paglione, J.; Rodriguez, E. E. Superconductivity and magnetism in iron sulfides intercalated by metal hydroxides. *Chem. Sci.* **2017**, *8*, 3781−3788.
(15) Wyckoff, R. *Crystal Structures*; Wiley, 1963; Vol. *1*.
(16) Desgranges, L.; Calvarin, G.; Chevrier, G. Interlayer interactions in $M(OH)_2$: a neutron diffraction study of Mg (OH) 2. *Acta Crystallogr., Sect. B: Struct. Sci.* **1996**, *52*, 82−86.
(17) Chen, Y.; Lu, J.; Gao, Z. Structural and electronic study of nanoscrolls rolled up by a single graphene sheet. *J. Phys. Chem. C* **2007**, *111*, 1625−1630.
(18) Tremel, W. Inorganic nanotubes. *Angew. Chem., Int. Ed.* **1999**, *38*, 2175−2179.
(19) Murr, L.; Soto, K. TEM comparison of chrysotile (asbestos) nanotubes and carbon nanotubes. *J. Mater. Sci.* **2004**, *39*, 4941−4947.
(20) Barrer, R. M. Mineral Synthesis by the Hydrothermal Technique. *Chem. Br.* **1966**, *2*, 380.
(21) Demazeau, G. Solvothermal reactions: an original route for the synthesis of novel materials. *J. Mater. Sci.* **2008**, *43*, 2104−2114.
(22) Modeshia, D. R.; Walton, R. I. Solvothermal synthesis of perovskites and pyrochlores: crystallization of functional oxides under milder conditions. *Chem. Soc. Rev.* **2010**, *39*, 4303−4325.
(23) Cundy, C. S.; Cox, P. A. Hydrothermal Synthesis of Zeolites: History and Development from the Earliest Days to the Present Time. *Chem. Rev.* **2003**, *103*, 663−701.
(24) Chen, X.-M.; Tong, M.-L. Solvothermal in situ metal/ligand reactions: A new bridge between coordination chemistry and organic synthetic chemistry. *Acc. Chem. Res.* **2007**, *40*, 162−170.
(25) Chirayil, T.; Zavalij, P.; Whittingham, M. S. Hydrothermal Synthesis of Vanadium Oxides. *Chem. Mater.* **1998**, *10*, 2629−2640.
(26) Byrappa, K.; Adschiri, T. Hydrothermal technology for nanotechnology. *Prog. Cryst. Growth Charact. Mater.* **2007**, *53*, 117−166.

https://dx.doi.org/10.1021/acs.chemmater.9b04121
Chem. Mater. 2020, 32, 769−775